

Supporting Information

Reversible Pressure-induced Partial Phase Transition in Few-Layer Black Phosphorus

Anirban Kundu,^{†,‡,||} Damien Tristant,^{¶,§,||} Natalya Sheremetyeva,[§] Anthony Yoshimura,[§] Abraao Torres Dias,[‡] Kiran Shankar Hazra,^{*,†} Vincent Meunier,^{*,§} and Pascal Puech^{*,‡}

[†]*Institute of Nano Science and Technology, Habitat Center, Sector 64, Phase 10, Mohali, Punjab, 160062, India*

[‡]*Centre d'Elaboration des Matériaux et d'Etudes Structurales (CEMES), UPR-8011 CNRS, Université de Toulouse, Toulouse, France*

[¶]*Cain Department of Chemical Engineering, Louisiana State University, Baton Rouge, Louisiana 70803, United States of America*

[§]*Department of Physics, Applied Physics, and Astronomy, Rensselaer Polytechnic Institute, Troy, New York 12180, United States of America*

^{||}*A. Kundu and D. Tristant contributed equally to this work.*

E-mail: kiran@inst.ac.in; meuniv@rpi.edu; pascal.puech@cemes.fr

Phone: +91 172-2210074; +1 (518) 276-6310; +33 562257886

1 Determination of Applied Pressure

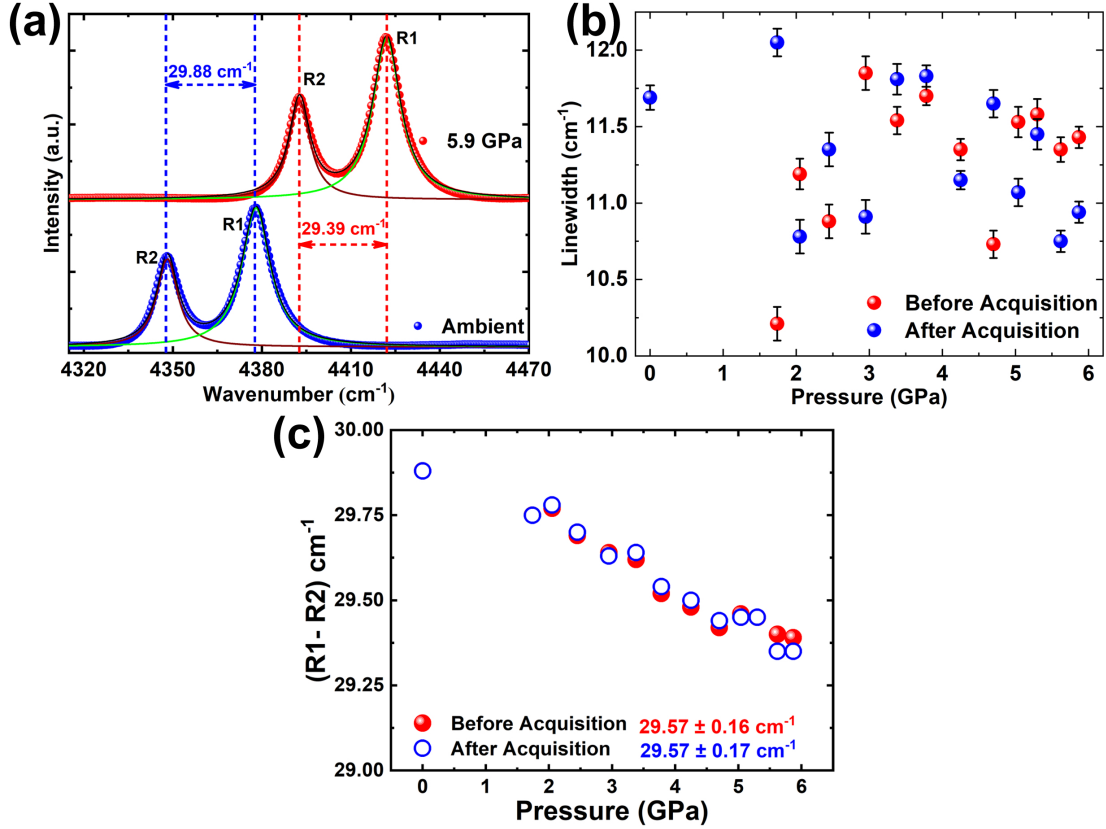


Figure S1: Experimental (a) Ruby PL lines at ambient pressure (blue line) and highest applied pressure $p = 5.87 \text{ GPa}$ (red line), (b) Linewidths of R1 and (c) Peak difference (R1-R2) with the variation of applied pressure remains constant over the applied pressure range with maximum standard deviation of $\pm 0.46 \text{ cm}^{-1}$ (linewidths) and $\pm 0.17 \text{ cm}^{-1}$ (peak difference), respectively.

In order to measure the applied pressure, a small piece of Ruby has been placed inside the diamond anvil cell (DAC) and PL spectra of Ruby line is recorded before and after the Raman spectra acquisition of the BP flake for each applied pressure to probe if there is a pressure variation during the measurements. The obtained PL spectra has been fitted with two Lorentzian functions to measure the peak positions, where the high energy PL peak has been used to calculate the applied pressure using the formula $p = (A/B)\{[1+(\Delta\lambda/\lambda_0)]^B - 1\}$, where $A = 19.04 \text{ Mbar}$, $B = 7.665$, $\Delta\lambda$ represents the shift in Ruby line, λ_0 is the Ruby

PL peak at ambient pressure, as reported by Mao *et. al.*¹. Figure S1a shows the typical PL spectra of Ruby lines at both ambient pressure and temperature. Each spectra has been fitted with two Lorentzian function to obtain the respective peak position, where the high energy peak is defined as R1 and the low energy one as R2. The obtained peak positions of R1 for each step of pressure are used to calculate the corresponding pressure. The average of the pressure value obtained before and after the acquisition is considered as the experimental applied pressure (p). It is well known that the maximum possible error during the estimation of pressure calculation is 5%, when the pressure is measured using the Ruby PL line. The maximum difference observed in pressure, before and after the acquisition, is equal to 0.12 GPa, which lies within the error range that confirms uniform pressure is maintained during the acquisition. The linewidths of the Ruby PL line (R1) over the all the applied pressure have been analyzed plotted in Figure S1b. The mean value with the standard deviation of the linewidth data is $11.3 \pm 0.5 \text{ cm}^{-1}$ corresponding to the Ruby PL peak recorded before the Raman spectra acquisition. Whereas the linewidth of R1 recorded after the Raman spectra acquisition is $11.3 \pm 0.5 \text{ cm}^{-1}$, which suggests that the Ruby linewidth remains constant throughout the pressure range and confirms the hydrostatic nature of the applied pressure. Apart from the linewidth, the peak difference of the two Ruby lines (R1-R2) has also been analyzed to confirm the hydrostatic nature of the applied pressure (Figure S1c), which shows that the mean peak difference obtained as $29.57 \pm 0.16 \text{ cm}^{-1}$ for the Ruby lines recorded before acquisition. Whereas the obtained mean peak difference for the Ruby lines recorded after the Raman acquisition is $29.6 \pm 0.2 \text{ cm}^{-1}$. This results shows that the peak difference of the Ruby PL lines remains constant over the complete pressure range. The analysis of linewidth along with the constant peak difference over the applied pressure range confirms the hydrostatic nature of the applied pressure inside the DAC.

2 Raman Spectrum

2.1 Fitted Raman Spectra of Layered BP Flake

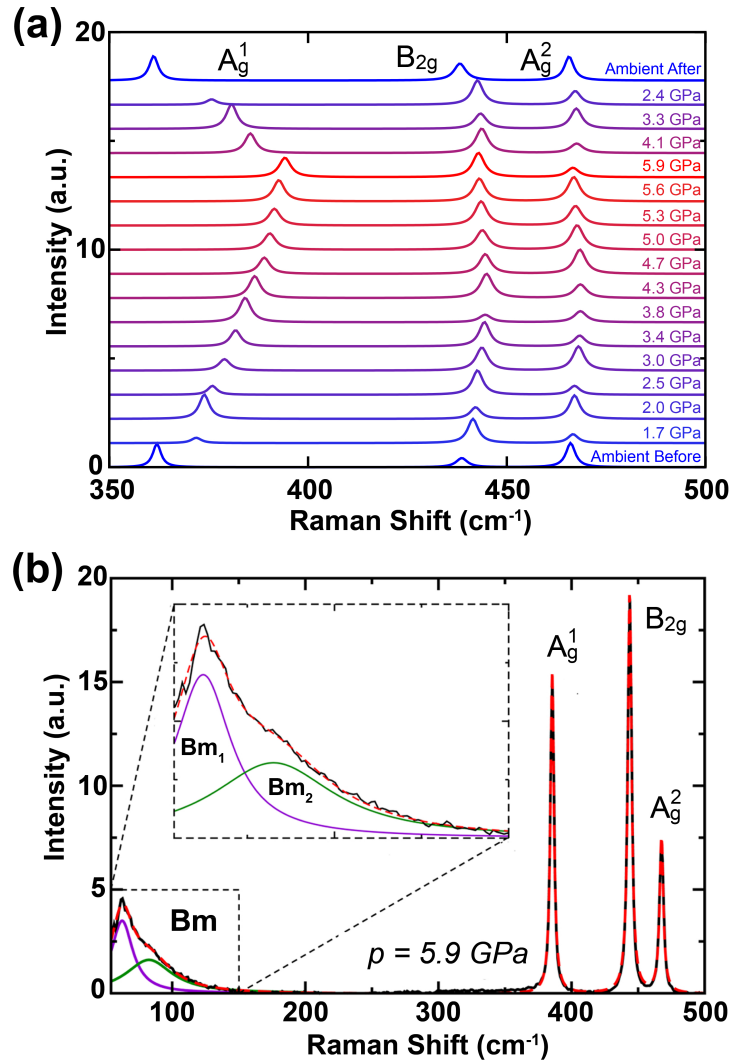


Figure S2: (a) Lorentzian fitted Raman spectra of BP flake at different applied pressure. (b) Experimental Raman spectrum at 5.9 GPa for few-layer black phosphorus (black line). The full spectrum is fitted with five Lorentzian functions (dashed red line). Inset: the zoom-in spectrum from 54 to 150 cm⁻¹, the green and blue lineshapes show the two fitted Lorentzian shape (one for the Bm mode (Bm₂ and the other is a combination of low frequency phonon modify by the notch filter Bm₂). The Rayleigh band is blocked by a Notch filter.

The experimentally observed Raman peaks are fitted with Lorentzian function to obtain the peak positions, where the fitted Raman spectra of the BP flake at different applied are shown in Figure S2a. Figure S2b shows the fitted Raman spectra of the BP flake at highest applied pressure $p = 5.9$ GPa.

2.2 Characterization of BP flake and Thickness Determination

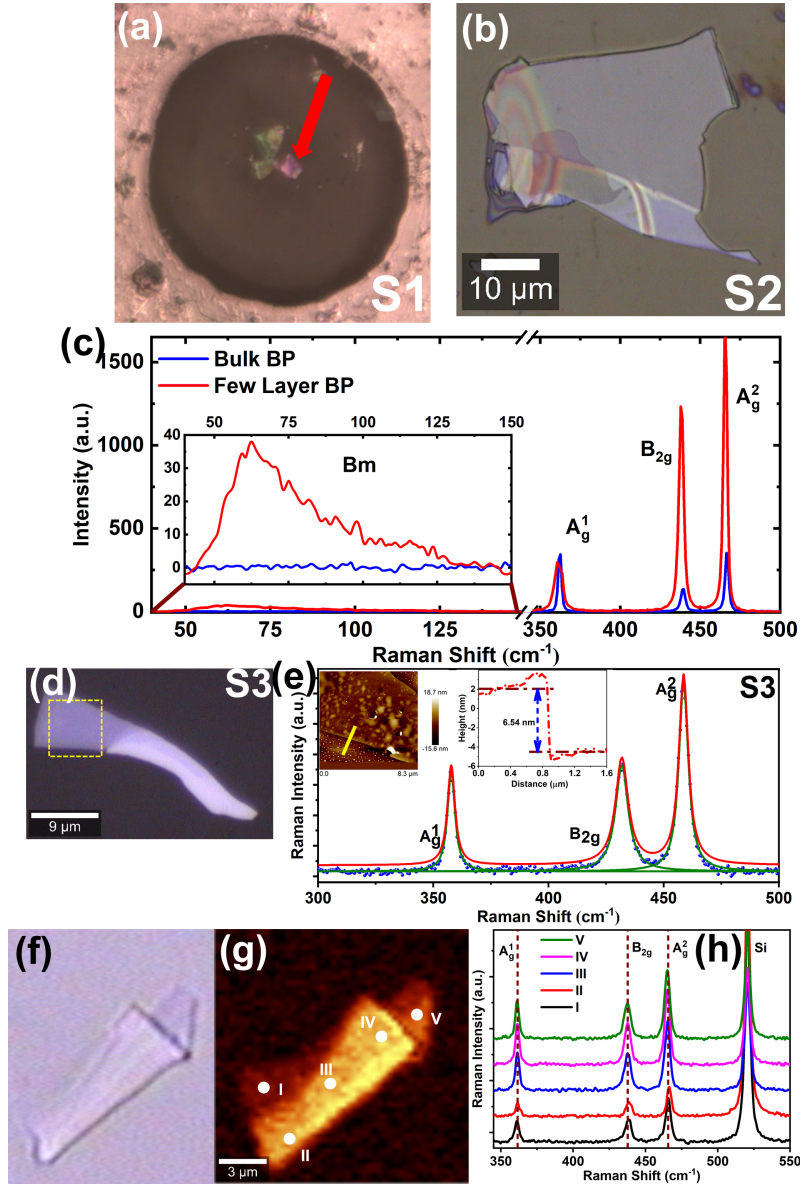


Figure S3: Optical image of (a) Few Layer BP flake inside DAC (denoted as S1) and (b) Typical bulk BP flake (denoted as S2). The arrow shows the part of the BP flake (S1) on which the High Pressure Raman spectra has been recorded. (c) Comparison of Raman spectra of few-layer (red line) and bulk BP (blue line) at 0 GPa showing the prominent breathing mode only observed in few-layer BP flake and (d) Optical image of BP flake for control experiment (denoted as S3) having similar optical contrast as compare to few layer BP flake (S1). (e) Raman spectra of the controlled BP flake (S3) and the Lorentzian fitted spectra. Inset shows the AFM height image of the area marked in the optical image (S3) and the height profile along the marked line in AFM height image.

In order to confirm the few layer nature of the BP flake used in High Pressure Raman measurement, a control experiments has been performed where the optical intensity profile and Raman spectroscopic analysis are employed to identify the layer number.²⁻⁶ The optical image of the BP flake (used for high pressure measurement; denoted by S1) and a typical bulk BP flake (denoted by S2) are shown in Figure S3(a-b). The marked arrow in Figure S3a shows the part of the flake on top of which the High Pressure Raman spectra were recorded by focusing the laser spot. The Raman spectra of the few layer BP flake (S1) in ambient condition is compared with the typical Raman spectra of a bulk BP flake (S2) (Figure S3c). Though both Raman spectra has been recorded using the same Raman spectrometer, no signature of low frequency Bm is observed for bulk BP, whereas a prominent low frequency Raman peak is observed in few layer BP flake. This could suggest that the observed low frequency Raman spectra is not the notch filter cut-off and solely originated due to the interlayer vibration of BP flake. The observed Raman peaks are fitted with Lorentzian function to obtain the peak positions. For instance, the characteristics Raman modes, *i.e.*, A_g^1 , B_{2g} and A_g^2 are observed at ~ 361.9 , ~ 438.7 and ~ 466.1 cm^{-1} for few-layer BP, whereas the Raman peaks are observed at ~ 362.1 , ~ 439.1 and ~ 465.8 cm^{-1} for bulk BP, respectively. As reported earlier,³ by analyzing the intensity ratio of A_g^2 and A_g^1 peak and the peak difference between A_g^2 and B_{2g} peak, the layer number in BP flake can be predicted. Here, the peak difference between A_g^2 and B_{2g} for few layer BP (~ 27.4 cm^{-1}) and bulk BP (~ 26.7 cm^{-1}) are comparable and may not confirm the few layer nature of the bP flake, but the higher value of $I(A_g^2/A_g^1)$ ratio for few layer BP (~ 2.67) compare to bulk BP (~ 1.15) confirms that the layer number in few layer flake less than 6. From the Raman signature (spectral positions and intensities), we estimate the number of layers to be around 5.

Along with the Raman measurement, the optical intensity profile has also been extracted to measure the optical contrast of the flake using the formula $\text{Contrast}(C) = \frac{I_{\text{substrate}} - I_{\text{sample}}}{I_{\text{substrate}}}$, where $I_{\text{substrate}}$ and I_{sample} are the reflected light intensities from the substrate and the sam-

Table S1: Calculated and reported parameters for layer number determination of BP flake

Sample	Optical Contrast	$I(A_g^2/A_g^1)$	$A_g^2-B_{2g}$ (cm^{-1})	Thickness	Layer Number
S1	0.47	2.67	27.4	-	≤ 6
S2	0.76	1.15	26.7	Bulk	Bulk
S3	0.41	2.52	27.6	6.54	~ 6
Reference ³	0.50	2.50	27.7	2.85	5
Reference ³	-	2.00	27.5	Bulk	Bulk

ple, respectively.^{5,7,8} The calculated optical contrast for few layer BP flake (S1) is obtained as ~ 0.47 , whereas the same for the bulk BP (S2) is ~ 0.7 . As reported earlier³, the optical contrast for BP flake with layer number ≤ 5 is lying in the range $\sim 0.15 - 0.50$, which also confirms that the few layer BP flake contains layers of less than 6. To achieve further confirmation of layer number of the few layer BP flake (S1), a similar BP flake has been transferred on Si substrate (denoted as S3) for control experiment (Figure S3d). The Raman spectra of the controlled flake is shown in Figure S3e, where the characteristics Raman modes *i.e.* A_g^1 , B_{2g} and A_g^2 are observed at ~ 359.5 , ~ 438.4 and ~ 465.9 cm^{-1} obtained by Lorentzian fitting of the spectra. By analyzing the Raman peaks positions and intensity, it has been observed that the peak difference between A_g^2 and B_{2g} is obtained as ~ 27.4 cm^{-1} and the $I(A_g^2/A_g^1)$ ratio is ~ 2.52 , which confirms that the layer number of the controlled BP flake is ≤ 6 . The layer number or thickness of the controlled BP flake has further been verified by measuring the AFM (Inset of Figure S3e), where the thickness is measured from the height profile as shown in the inset of Figure S3e. The height profile of the controlled flake confirms that the thickness of the BP flake is ~ 6.54 nm, which suggest that the number of layers present in that flake seems to be ≤ 6 . All the measured parameters corresponding to the three BP flakes *i.e.* S1, S2 and S3 are compared with the previous reported results by Lu *et. al.* in Table S1 for better understanding.

Figure S3f shows the optical image of a typical BP flake and the Raman mapping of the BP flake are shown in Figure S3g. The Raman spectra of the BP flake are extracted

from the different position of the flake as shown on the Raman mapping image. The Raman spectra recorded at different positions are compared to confirm the layer number independent Raman peak position of BP flake. The thickness variation of the flake is confirmed from the optical image and the mapping data only. The Raman spectra from three different points (II, III and IV) confirm that the intensity of the BP flake in that region is uniform for all three characteristics Raman modes (A_g^1 , B_{2g} and A_g^2), which cover nearly around 70% of the total flake. In consequence, it is possible to identify the homogeneous region from the optical image of the flake only, which is followed in our work.

2.3 Evolution of Low Frequency (LF) Raman Modes

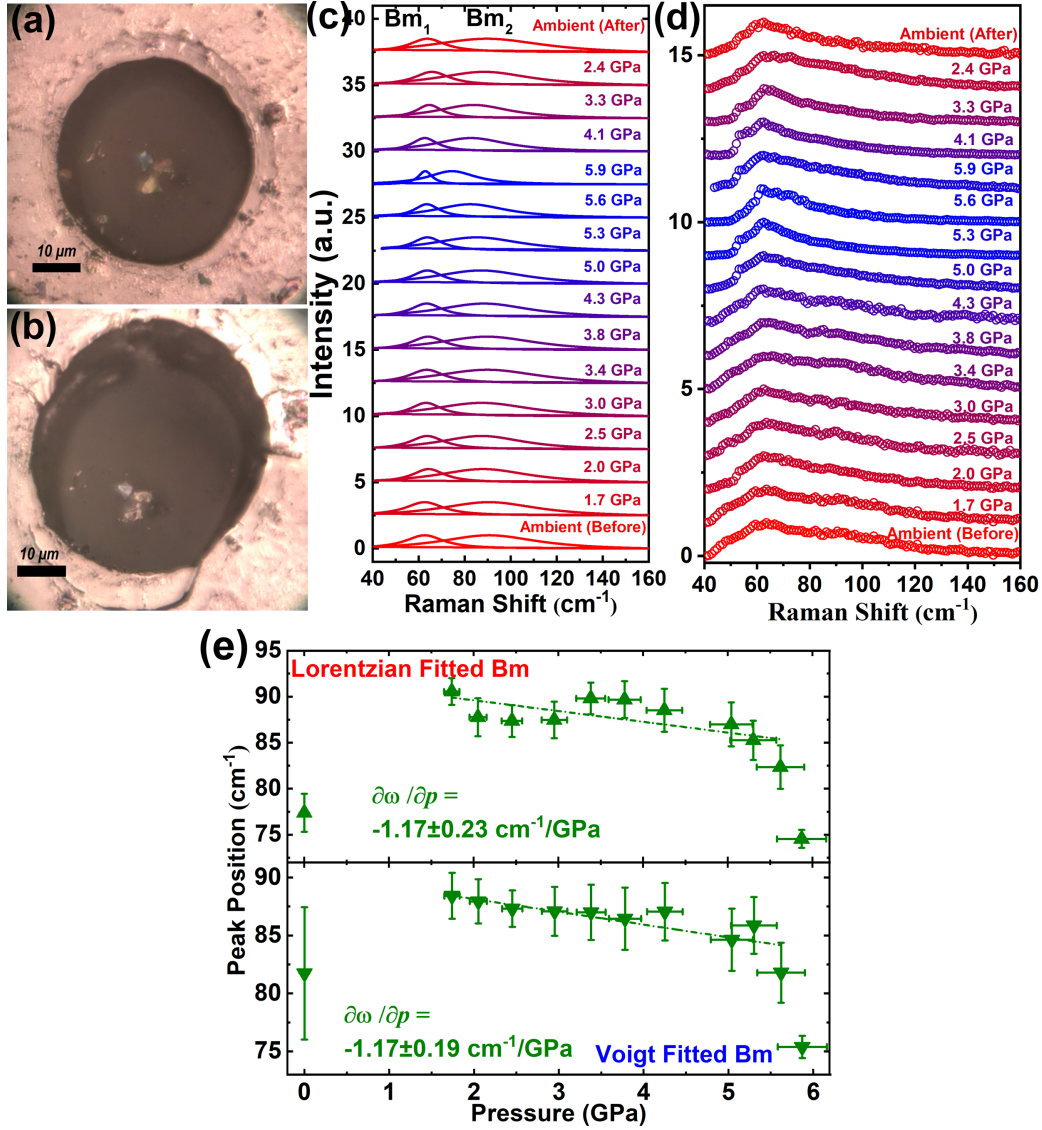


Figure S4: Typical optical images of few-layer black phosphorus (BP) inside a diamond anvil cell at (a) ambient pressure and (b) 5.9 GPa. (c) Evolution of the two low-frequency Raman modes (Bm₁ and Bm₂) of few-layer BP for different pressure values obtained normalization and fitting of the peaks with Lorentzian functions. For better visibility, the low-frequency breathing mode (Bm) is represented with a Lorentzian function. (d) Raman spectra at low frequency region showing the experimental data points. The Bm₁ mode could be suppressed by notch filter, that's why Bm₂ is considered as Bm only. (e) Pressure dependence of breathing mode (Bm) shift.

The optical image of the few-layer BP flake inside the DAC are shown in Figure S4a

and the circular shape of the gasket indicates a uniform distribution of applied pressure. This shape is slightly deformed at the highest applied pressure of 5.9 GPa (Figure S4b). In general, the LF interlayer modes have been shown to be more sensitive to structural changes in (multi-) layered materials than their high-frequency (HF) intralayer counterparts.⁹ They are also especially important for studying the weaker interlayer interactions that determine the restoring forces between layers.⁹ However, it is difficult to measure the evolution of low energy Raman peaks under high pressure as compare to the high frequency modes because of their proximity to the strong Rayleigh line. The deconvolution of the Raman spectra in Figure S4c shows that only two Raman peaks are observed in the LF region at 66 cm^{-1} (may not accurate due to the presence of a notch filter) (B_{m_1}) and 89 cm^{-1} (B_{m_2}), which provides further indication that the BP flake contains fewer than 6 layers. Since B_{m_1} is very close to Rayleigh line and could be suppressed by Notch filter cut off, hence in order resolve any kind of ambiguity only the B_{m_2} has been considered (henceforth denoted as Bm), which is a clear and prominent hump of the spectra and significantly away from the cut off. The corresponding Lorentzian fitted $\partial\omega/\partial p$ slope enable a more quantitative view on how Bm evolves under applied pressure (Figure S4), where the quasi-linear part of the pressure dependency data is considered as major portion to determine the $\partial\omega/\partial p$. The Raman peak position of the Bm mode $\sim 89\text{ cm}^{-1}$ decreases at a rate of $-1.17\pm 0.23\text{ cm}^{-1}/\text{GPa}$ in the pressure range [1.7, 5.6] GPa. To double check the evolution of the Bm, the low frequency Raman modes are fitted with *Voigt* function as well and corresponding evolution of Bm is shown in Figure S4e, which also depicts the same $\partial\omega/\partial p$ as observed for Lorentzian fitted peak positions. Hence it is well conclusive that the Bm peak is originating solely from the breathing mode Raman signal and the error bars, as shown in Figure S4e, suggest that the trend of redshift is prominent and beyond the signal fluctuation error. This experimentally obtained $\partial\omega/\partial p$ is well complemented by the theoretically predicted slope ($-4.28\pm 0.12\text{ cm}^{-1}/\text{GPa}$), as both the value suggests that the breathing mode shows redshift with the increasing applied

pressure. A few reports on layered materials, such as graphite, show that its breathing modes are redshifted upon applying uniaxial and hydrostatic pressure.¹⁰ In the case of few-layer MoS₂ and WTe₂, a blueshift is observed for lower energy Raman vibrational modes as well as with increasing applied pressure.^{11,12} This blueshift is in clear departure from the observed redshifts in breathing modes of few-layer BP flake. These results may be attributed to the decrease in effective interlayer distance and enhancement of intralayer distance in case of the BP flake, as shown in Table S2.

2.4 Linewidth and Phonon Lifetime Under Applied Pressure

Pressure-dependent Raman linewidths are plotted in Figure S5(a), which shows that the linewidths of all the characteristic Raman modes increase with increasing applied pressure. For instance, with applied pressure of 5.9 GPa, the A_g^1 , B_{2g} , and A_g^2 Raman modes are broadened by 1.07, 0.17, and 0.89 cm^{-1} , respectively, as compared to those measured at ambient pressure. The increase in the linewidths of the Raman modes confirms a wide distribution of phonon energy, which possibly attributable to enhanced electron-phonon (e -ph) interactions. This enhancement can be confirmed by calculating the e -ph coupling parameter, D , from the linewidth broadening given as:^{13,14}

$$\Delta\Gamma = \frac{A_{\text{uc}}}{8Mv_{\text{F}}^2}D^2, \quad (1)$$

where A_{uc} is the area of the single-layer black phosphorus unit cell, M is the mass of the phosphorus atom, v_{F} is the Fermi velocity ($\sim 8 \times 10^5 \text{ m s}^{-1}$). The enhancement in e -ph interactions also reduces the phonon lifetime, τ , which can be derived from the energy uncertainty relation with the phonon linewidth, Γ :^{15,16}

$$\tau = \frac{\hbar}{\Gamma}, \quad (2)$$

where \hbar is the reduced Planck constant. The phonon lifetime corresponding to each characteristics vibrational mode is plotted in Figure S5(b), where the A_g^1 , B_{2g} and A_g^2 Raman modes show significantly reduced phonon lifetimes of 650, 80, and 450 fs, respectively, when the applied pressure increases to 4.2 GPa from ambient pressure. Such decreases in phonon lifetime can be explained from the enhancement of the e -ph coupling parameter, as the probability of e -ph coupling increases with increasing applied pressure. Pressure-dependent enhancement in e -ph interactions also indicates that the electrical conductivity of BP must depend on external pressure, which is in good agreement with results reported previously.¹⁷⁻¹⁹

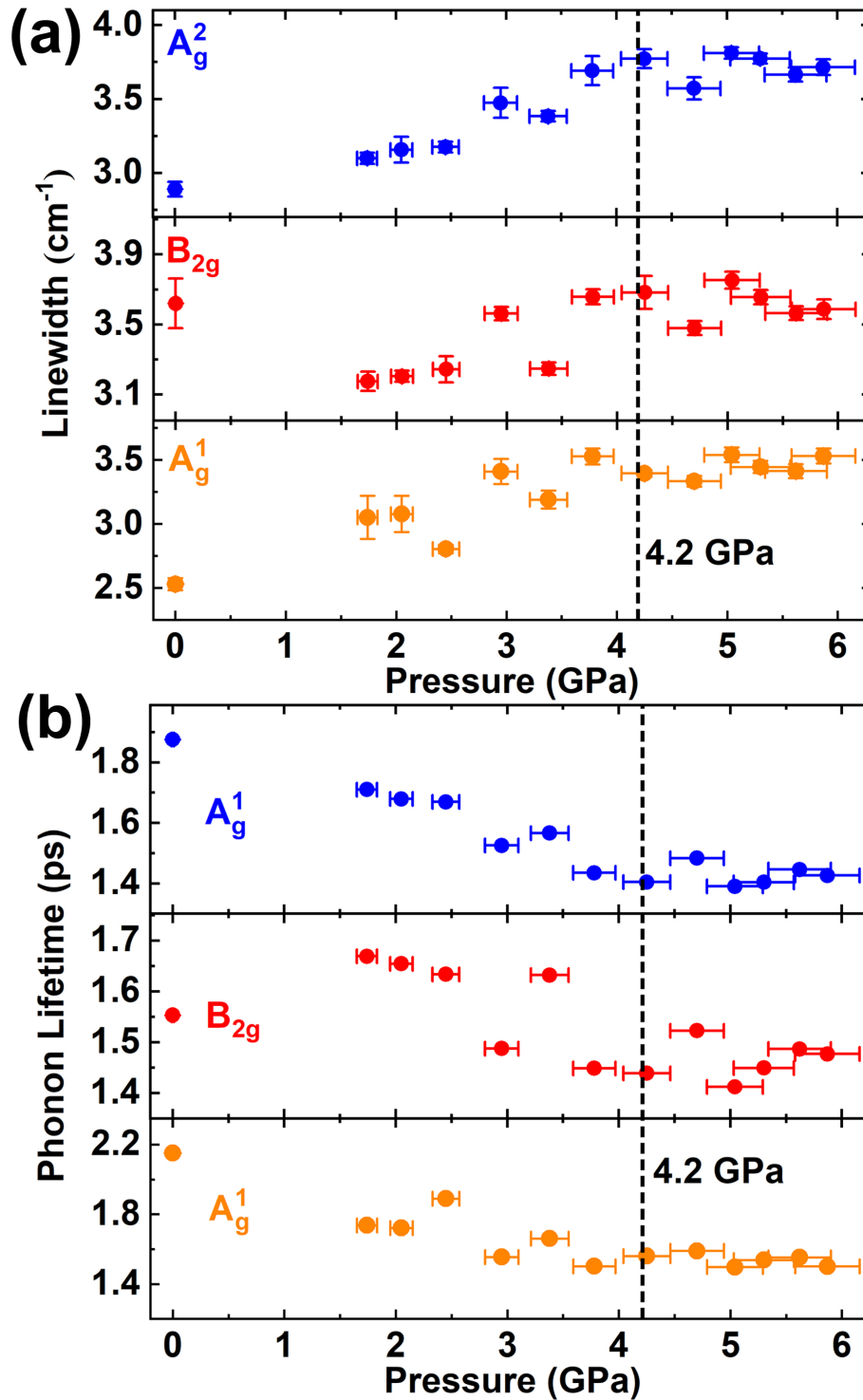


Figure S5: Pressure dependence of (a) linewidth, and (b) phonon lifetime for few-layer black phosphorus flake. The frequency transition pressure at 4.2 GPa is represented by a dashed black line. The applied pressure starts from 1.74 GPa.

2.5 Modified Raman Spectra at High Pressure

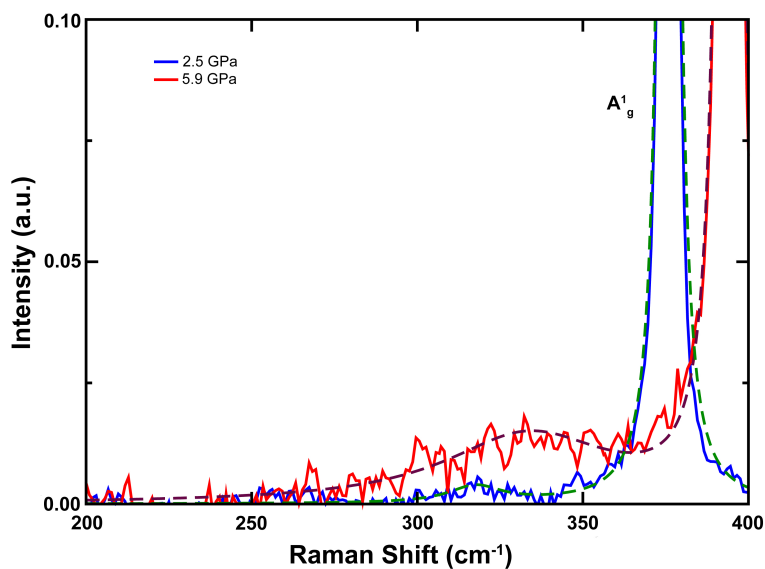


Figure S6: Experimental Raman spectra at 2.5 and 5.9 GPa for few-layer black phosphorus (solid line). Each spectrum is fitted with two Lorentzian functions (dashed line).

Figure S6 reports the modification of the HF range under pressure after the partial transition.

3 First Principle Calculation

3.1 Hydrostatic and Uniaxial Pressure Methods

The stress at any point in a continuous body is described by a stress tensor

$$\sigma = \begin{pmatrix} \sigma_{11} & \sigma_{12} & \sigma_{13} \\ \sigma_{21} & \sigma_{22} & \sigma_{23} \\ \sigma_{31} & \sigma_{32} & \sigma_{33} \end{pmatrix}, \quad (3)$$

where

$$\sigma_{ij} = \frac{dF_i}{dS_j} \quad (4)$$

is the force per unit area that acts in the i th Cartesian direction on a surface element oriented in the direction normal to the j th dimension. The form of the stress tensor is significantly simplified if the properties of the body and conditions in which the stress is applied obey certain symmetries. For example, the stress in a static fluid is both rotationally and translationally invariant. Its magnitude is therefore independent on the direction and position, and the direction in which it acts must be perpendicular to the surface on which it is applied. The hydrostatic stress (HS) tensor thus takes the form

$$\sigma_{\text{HS}} = \begin{pmatrix} p & 0 & 0 \\ 0 & p & 0 \\ 0 & 0 & p \end{pmatrix}, \quad (5)$$

where p is the pressure of the fluid. The elements of the stress tensor are similarly constrained in a homogeneous rigid body under a uniform external stress. In this case, the stress at any point in the body is again position-independent, but only acts along one direction, which we

designate as $\hat{\mathbf{z}}$. We can therefore write the uniaxial stress (US) tensor as

$$\sigma_{\text{US}} = \begin{pmatrix} 0 & 0 & 0 \\ 0 & 0 & 0 \\ 0 & 0 & p \end{pmatrix}, \quad (6)$$

where p is now the external pressure applied to the rigid body.

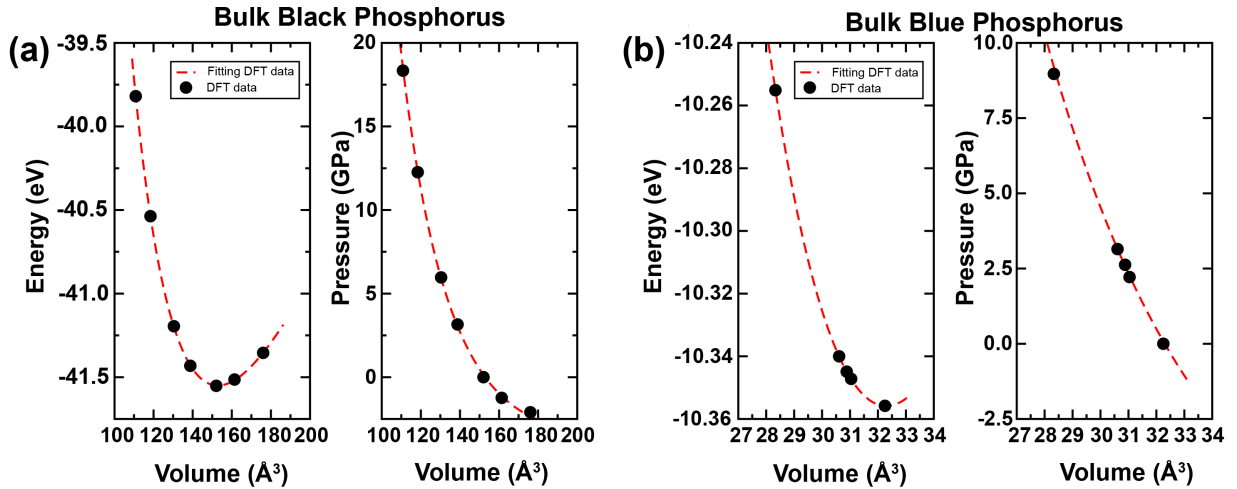


Figure S7: Volume dependence of (left panel) the ground state energy and (right panel) hydrostatic pressure of bulk (a) black and (b) blue phosphorus. Density functional theory (DFT) data are interpolated using the Birch-Murnaghan equations.^{20,21}

In a computational simulation, a periodic system under stress is modeled by tuning the magnitudes and directions of the lattice vectors so that the change in energy with respect to unit cell dimensions agrees with the corresponding element in the stress tensor. Here, we use DFT to obtain the necessary relationships between energy and lattice vectors.

To simulate hydrostatic pressure, we allow all atoms and lattice vectors of bulk BP to relax while constraining the volume of the unit cell. In this way, the lattice vectors will be modified until the pressure on all unit cell faces is uniform and any shearing forces disappear, so that the stress tensor takes the hydrostatic form of Eq. (5) in the manuscript. We obtain the ground state energies in this way for a series of unit cell volumes. We then fit the

Table S2: Calculated intralayer and interlayer distances (\AA) of bulk black phosphorus under hydrostatic pressure (GPa).

Pressure	Intralayer distance	Interlayer distance
0	2.164	3.088
0.941	2.169	3.005
2.002	2.174	2.931
3.103	2.179	2.877
4.114	2.183	2.830
5.087	2.188	2.795
6.044	2.192	2.763

Birch-Murnaghan isothermal equation of state given by^{20,21}

$$E(V) = E_0 + \frac{9V_0B_0}{16} \left\{ \left[\left(\frac{V_0}{V} \right)^{\frac{2}{3}} - 1 \right]^3 B'_0 + \left[\left(\frac{V_0}{V} \right)^{\frac{2}{3}} - 1 \right]^2 \left[6 - 4 \left(\frac{V_0}{V} \right)^{\frac{2}{3}} \right] \right\}, \quad (7)$$

to these points in energy-volume space, as shown in left panel of Figure S7(a). With the fitted parameters, *i.e.*, the equilibrium energy (E_0) and volume (V_0) at zero pressure, and the equilibrium bulk modulus (B_0) and its first derivative with respect to the pressure (B'_0), we choose the lattice vectors that best describe bulk BP subjected to a desired pressure. This is achieved by setting the unit cell to the corresponding volume predicted by^{20,21}

$$p(V) = \frac{3B_0}{2} \left[\left(\frac{V_0}{V} \right)^{\frac{7}{3}} - \left(\frac{V_0}{V} \right)^{\frac{5}{3}} \right] \left\{ 1 + \frac{3}{4}(B'_0 - 4) \left[\left(\frac{V_0}{V} \right)^{\frac{2}{3}} - 1 \right] \right\}, \quad (8)$$

Figure S7(b) shows the volume dependence of the ground state energy and hydrostatic pressure of bulk blue Phosphorus (bP). The fitting parameters extracted from Eq. (7) for BP and bP are summarized in Table S3.

Table S3: Equilibrium ground state energy E_0 (eV) and volume V_0 (\AA^3) at zero pressure, and equilibrium bulk modulus B_0 (GPa) and its first derivative with respect to the pressure B'_0 , extracted from the Birch-Murnaghan isothermal equation of state.^{20,21} These calculations are obtained for bulk black (BP) and blue (bP) phosphorus. Available experimental value from the literature is reported in parentheses.²²

Structure	E_0	V_0	B_0	B'_0
BP	-41.55	153.000	24.259 (32.5)	5.223
bP	-10.36	32.300	51.779	4.615

Figure S8 shows the vibrational band structure of BP at zero pressure (black solid lines) compared to that at 3 GPa (dashed red lines) along the high-symmetry lines in the first Brillouin zone (BZ). The primitive cell of AB-stacked bulk BP contains four atoms considering that the orthorhombic unit cell of AB-stacked bulk BP contains eight atoms can be reduced to a primitive cell with only four atoms. Thus, the phonon band structure of BP has 12 branches: three of which are acoustic and nine are optical. The overall shape of the vibrational bands remains the same under applied pressure. However, most vibrational frequencies of BP at the Γ -point are slightly blue-shifted under pressure.

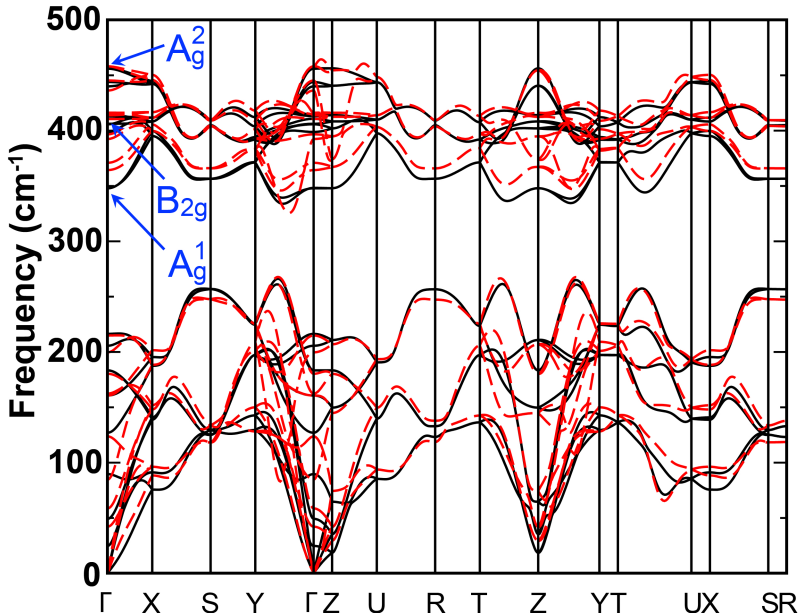


Figure S8: Vibrational band structure of bulk black phosphorus (BP) at 0 GPa (black solid lines) and 3 GPa (dashed red lines). These calculations are based on hydrostatic pressure method and the distances between high-symmetry points have been renormalized.

The simulation of uniaxial pressure cannot allow the lattice vectors relax as they did in the hydrostatic pressure simulation. This is because the applied stress is no longer isotropic. Instead, supposing that a nonzero external stress acts along the out-of-plane lattice vector \mathbf{c} , the in-plane lattice vectors \mathbf{a} and \mathbf{b} will relax until all in-plane stress disappears, and the stress tensor takes the uniaxial form of Eq. (6) in the manuscript.

Given that bulk BP possesses an orthorhombic lattice, and that the applied stress is parallel to \mathbf{c} , we posit that the three lattice vectors will remain mutually orthogonal for any amount of applied stress. We therefore need only consider the magnitudes of the lattice vectors, a , b , and c , from here on out. It follows that, before a and b change in response to the external pressure, the stress tensor can be written as

$$\sigma_{\text{US}} = \begin{pmatrix} p_x & 0 & 0 \\ 0 & p_y & 0 \\ 0 & 0 & p_z \end{pmatrix}, \quad (9)$$

where each diagonal element p_i is the pressure exerted on a surface normal to the i th direction.

For a given c , we relax the system with fixed lattice vectors for several pairs of a and b values. Each pair (a, b) gives a set of pressures p_x , p_y and p_z . We fit p_x and p_y separately as functions of both a and b with the two-dimensional quadratic functions:

$$\begin{cases} P_{11} + P_{12}a + P_{13}b + P_{14}a^2 + P_{15}ab + P_{16}b^2 = 0 \\ P_{21} + P_{22}a + P_{23}b + P_{24}a^2 + P_{25}ab + P_{26}b^2 = 0 \end{cases}, \quad (10)$$

where P_{ij} are the fitted parameters. Solving the fitted p_x function for $p_x = 0$ yields a curve $a_{0,x}(b)$ on the $p_x = 0$ plane, while solving for $p_y = 0$ to yields the curve $a_{0,y}(b)$. The intersection of these two curves approximates the values of a_0 and b_0 for which both p_x and p_y disappear. These are the first-iteration approximations for the in-plane lattice parameters assumed by bulk BP under uniaxial pressure. We then relax a new system with lattice parameters a_0 and b_0 and add the resulting p_x and p_y to the previous set of pressures. Re-fitting the quadratic functions yields new values of a_0 and b_0 . Presumably, by repeating this process, the values of p_x and p_y will both approach zero through successive iterations. We continue in this way until both p_x and p_y fall below 10^{-4} GPa. The above process is carried

out for seven c values to simulate a sufficiently wide range of applied pressures. We note that because bulk BP has orthorhombic symmetry, we can choose \mathbf{c} to point out-of-plane, parallel to the stress. Therefore, we can change the magnitude of the stress simply by changing c . However, generally speaking, one should adjust the lattice parameters so that the scaling of the unit cell is parallel to the stress. Clearly, in a non-orthorhombic system, such as bP, this scaling can require changes in more than one lattice parameter.

3.2 Hydrostatic Pressure Dependent Lattice Parameters of black phosphorus (BP) and blue phosphorus (bP)

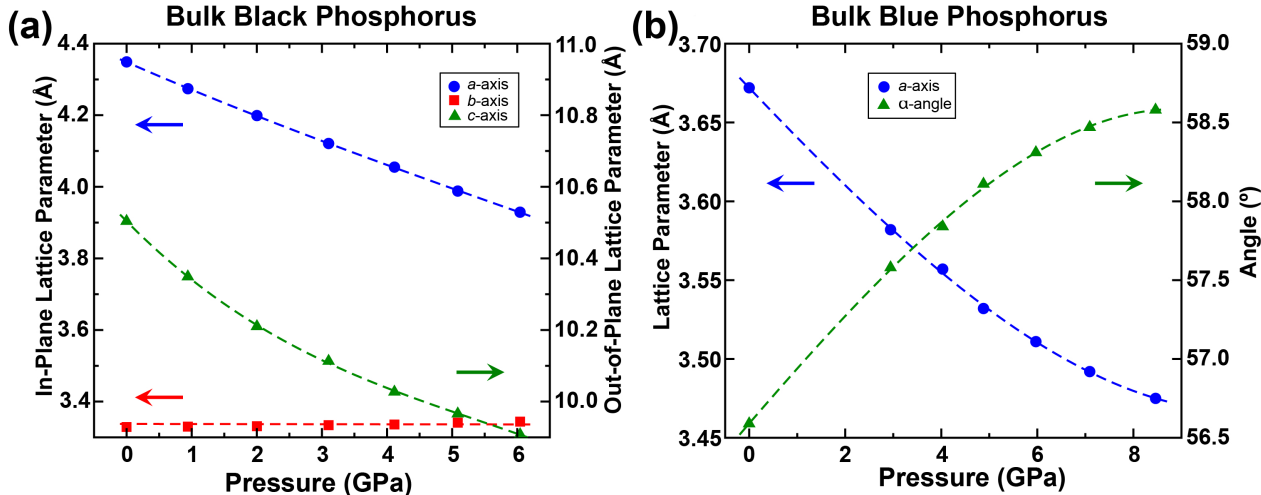


Figure S9: Hydrostatic pressure dependence of the lattice parameters of bulk (a) black phosphorus and (b) blue phosphorus (bP). Bulk bP has a rhombohedral structure, *i.e.*, $a = b = c$ and $\alpha = \beta = \gamma$. Values are interpolated with a third degree polynomial function (dashed lines).

The lattice parameters of BP are calculated to be $a = 4.349 \text{ \AA}$ (in-plane armchair), $b = 3.329 \text{ \AA}$ (in-plane zigzag), and $c = 10.504 \text{ \AA}$ (out-of plane direction) at zero temperature and zero pressure. These lattice parameters are in excellent agreement with reported experimental data, with the largest deviation being -0.6% for the a -axis constant (armchair direction).²²⁻²⁴ To develop understanding of the pressure induced structural changes, the lattice parameters are then calculated for seven values of hydrostatic pressure of bulk BP as plotted in Figure S9a. The hydrostatic pressure dependence of the lattice parameters of bulk BP shows that an increase in pressure drastically compresses the lattice parameters a and c , while b remains almost unchanged, even increasing slightly by 0.15% . This anisotropy in the in-plane compressibility of the lattice constant arises from the highly anisotropic atomic arrangement of BP,²⁵ for which compression in the a direction causes the in-plane bonds to rotate so that their alignment with the b direction increases. Bulk bP was first predicted

computationally and very recently experimentally realized on Au(111) substrate.^{26,27} The computationally optimized lattice parameters of bulk bP are $a = b = c = 3.672 \text{ \AA}$, and $\alpha = \beta = \gamma = 56.59^\circ$, which are in good agreement with previously reported values.²⁸ The hydrostatic pressure dependence of the lattice parameters of bP are depicted in Figure S9b. It shows that an increase in pressure induces a compression of the magnitude of the lattice vectors $a = b = c$, while the angles $\alpha = \beta = \gamma$ increase.

3.3 Uniaxial Pressure dependent Lattice parameter of bulk black phosphorus (BP)

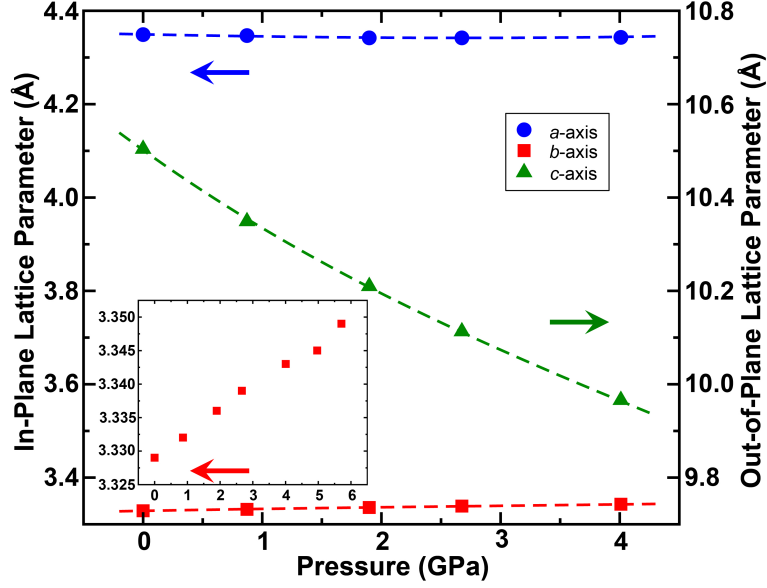


Figure S10: Uniaxial pressure-dependence of the lattice parameters of bulk black phosphorus. Values are interpolated with third degree polynomial functions (dashed lines).

Table S4: Uniaxial pressure-dependence (GPa) of the lattice parameters (Å) of bulk black phosphorus. These values are associated with Figure S10

Pressure	<i>a</i>	<i>b</i>	<i>c</i>
0.00	4.349	3.329	10.504
0.87	4.347	3.332	10.349
1.90	4.342	3.336	10.210
2.67	4.342	3.339	10.113
4.01	4.343	3.343	9.966
4.97	4.351	3.345	9.858
5.71	4.354	3.349	9.788

4 Theoretical Modeling of Phase Transition Point

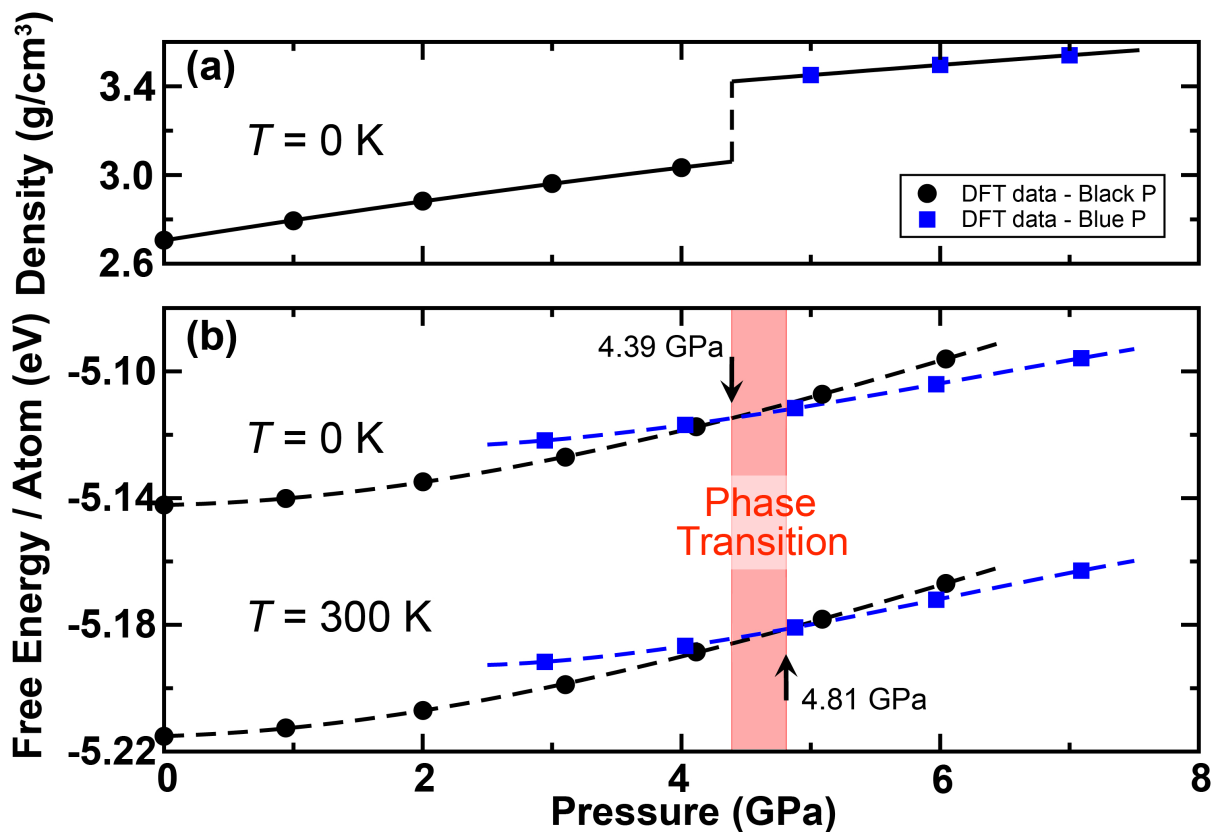


Figure S11: Hydrostatic pressure dependent (a) Density of the most stable phase (BP & bP) and (b) Helmholtz free energy per P atom for bulk black (BP) and blue (bP) phosphorus, at 0 K (including zero point energy) and 300 K. The phase transition pressure between bulk BP and bP ranges from 4.39 GPa (0 K) to 4.81 GPa (300 K).

Experimentally, BP is known to undergo a phase transition to the bP form at an elevated pressure of ~ 4.5 GPa,^{18,29–32} which is also observed in the experimental results reported here. The phase transition of BP into bP can be theoretically modeled by examining the density of the most stable phases (Figure S11a) and the competing energetics of the two phosphorus phases (BP and bP) under hydrostatic pressure conditions. Figure S11b shows the calculated Helmholtz free energies (including the zero point energy and the entropic contribution) per P atom of BP and bP as a function of pressure for two different temperatures, at 0 and 300 K. Comparing the energetics of BP and bP, a range of pressure is predicted under which the

phase transition can occur. At 0 K, it can be observed that bP becomes more stable than BP at pressures above 4.39 GPa, whereas this transition pressure shifts to 4.81 GPa at 300 K. The observed experimental transition pressure falls within the same pressure range, thus validating DFT's ability to accurately model the experimental conditions.

It is well-known that the change in temperature induces a shift in the phonon frequencies due to phonon-phonon (ph-ph) coupling. Such shift in phonon frequencies can be measured both experimentally by Raman spectroscopy coupled to a cryostat and theoretically using *ab initio* molecular dynamics simulations or many-body perturbation theory.³³ At room temperature and zero pressure, the frequencies of Raman-active modes in few-layer BP are downshifted by $\sim 2 \text{ cm}^{-1}$ from those obtained at zero temperature. Here, the possibility of ph-ph scattering has been neglected by assuming that the most important contribution to the frequency shifts originates from pressure variations only. Subsequently, all calculations were performed at zero temperature, taking into consideration only the ground state energy.

5 Uniaxial Pressure Dependent Raman Spectra of BP

For the sake of comparison, the HF modes of bulk BP have also been calculated under the uniaxial pressure conditions along z -direction. The uniaxial pressure method and dependence of the lattice parameters of bulk BP are detailed in Figure S8. Surprisingly, the lattice constant along the armchair direction behaves non-monotonically as the pressure increases. Such non-monotonic behavior of the lattice constant may originate from the particular puckered atomic arrangement of BP, which leads to the minimization of its inter-atomic repulsion by decreasing the lattice constant a at an applied uniaxial pressure of 3 GPa. In a theoretical calculation, Jiang *et al.* have obtained a negative Poisson's ratio for single-layer BP in the out-of-plane direction under uniaxial pressure in the direction parallel to the puckered arrangement.³⁴ In fact, when a bond angle is opened along the zigzag direction, another bond angle closes along the armchair direction, which results in the expansion of the lattice constants in the out-of-plan direction. Figure S9 shows the uniaxial pressure dependence of the HF characteristic Raman modes, which reveals that at low pressure range, the linear behavior of A_g^1 mode is identical to that obtained when the applied pressure is hydrostatic (Figure S12a). However, the $\omega(p)$ trend of B_{2g} and A_g^2 modes are non-monotonic with a strong redshift up to 2 GPa and above which the frequencies become blueshifted, which contradicts the experimental data. As a result, it can be concluded that the pressure applied on the bulk BP sample in our experiment is purely hydrostatic, which is also been verified experimentally by analyzing the linewidths and peak differences of the Ruby PL lines (Figure S1).

Theoretically, it has been predicted that bulk BP undergoes a phase transition to the bP form at ~ 4.39 GPa (at zero temperature), while experimentally a Raman signature of phase transition is measured at ~ 4.2 GPa. Though it is worth to mention that experimentally no prominent Raman peak corresponding to bP (rhombohedral crystal structure) is

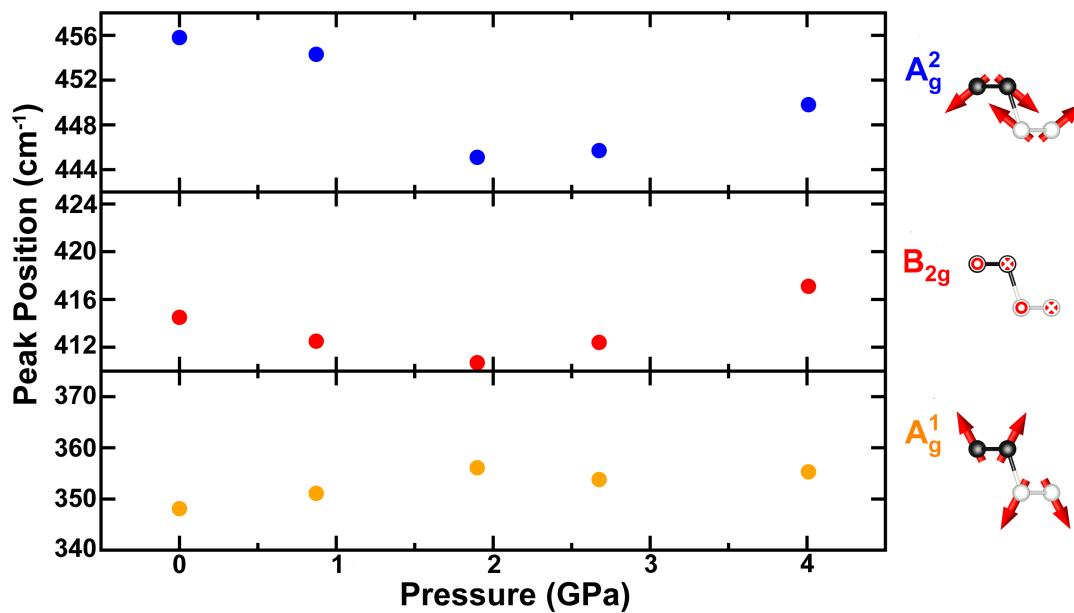


Figure S12: Uniaxial pressure-dependence of harmonic high-frequency shift for bulk black phosphorus. Vibrations of high-frequency intralayer modes, A_g^1 (out-of-plane), B_{2g} (along zigzag direction), and A_g^2 (along armchair direction) are shown on the right of each panel. The cross and circle indicate vibrations going into and out of the plane of the page, respectively.

observed.^{18,29} However, a difference between the Raman spectra in the range of [300,350] cm^{-1} is obtained for pressure values of 2.5 GPa and 5.9 GPa where a small Raman signal appears at $\sim 335 \text{ cm}^{-1}$ for an applied pressure of 5.9 GPa, as shown in Figure S5. Therefore, it is necessary to extend our structural and vibrational study to investigate bulk bP under high hydrostatic pressure ($\geq 3 \text{ GPa}$).

6 Hydrostatic Pressure Dependent Low-Frequency (LF) Raman Modes

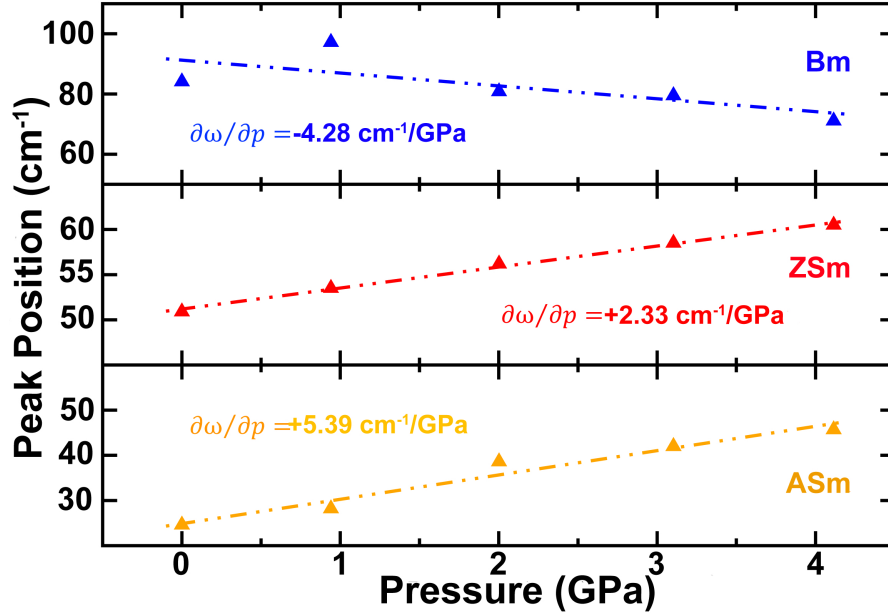


Figure S13: Hydrostatic pressure dependence of harmonic low-frequency shift for bulk black phosphorus. The hydrostatic pressure dependence of the frequency mode at low pressure is represented by the dashed-dotted colored lines.

Subsequently, in order to understand the evolution of LF Raman modes, the LF modes are also determined from the first-principles DFT. Bulk BP (*i.e.* AB-stacked bilayers in primitive cell) possesses one Bm and two shearing modes (Sm): one along zigzag direction (ZSm) and another in armchair direction (ASm). Figure S13 depicts the calculated Raman modes for the LF interlayer modes under various applied pressures. It shows that both the Sm behave similarly to one another, in fact their frequencies increase almost linearly with increasing pressure up to the point where a phase transition is predicted, *i.e.*, at 4.39 GPa. The linear fits of the $\omega(p)$ curves in the region [0,4] GPa yield a $\partial\omega/\partial p$ slopes of +2.33 and +5.39 $\text{cm}^{-1}/\text{GPa}$ for ASm and ZSm, respectively (Figure S13). On the other hand, Bm behaves distinctly from the Sm as its frequency decreases over the pressure range [0,4] GPa at a rate

of $-4.28 \text{ cm}^{-1}/\text{GPa}$. This is at first surprising, as one might expect the Bm, which essentially probes the out-of-plane interlayer distance in layered structures, to blueshift strongly as the out-of-plane lattice constant c decreases with increasing pressure (Figure S9a and Table S1). Instead, Figure S13 shows a strong redshift with increasing pressure starting from 1 GPa. Interestingly, the frequency of the breathing mode is first blueshifted by $\sim 13 \text{ cm}^{-1}$ at 1 GPa from its value at zero pressure. The inversion of $\partial\omega/\partial p$ for the Bm mode is also observed experimentally in Figure S3, granted the LF peaks are much broader than those of HF. Similarly to the case of HF modes, the counter-intuitive behaviour of Bm might again be attributed to the even more important role of short-range van der Waals (vdW) interactions between the layers, which are in good agreement with the previously reported results.^{2,35-37} The theoretically predicted (using optB88-vdW scheme) Bm appears at $\sim 89.1 \text{ cm}^{-1}$, which is in agreement with the experimentally fitted peak at $\sim 86 \text{ cm}^{-1}$ (Figure S2).

7 Electronic Properties of Bulk Black Phosphorus Under Hydrostatic Pressure

In parallel to the calculation of phonon frequencies, the electronic band gap of bulk BP has also been estimated using a hybrid DFT functional. At zero pressure, the calculated electronic band structure, Figure S14, indicates that the bulk BP is a semiconductor with a direct electronic band gap, $E_g = 0.37$ eV, located at the Γ -point. This result is in excellent agreement with the measured bulk band gap value, 0.31 – 0.36 eV.^{38–40} Thereafter, we study the E_g behaviour of bulk BP under applied hydrostatic pressure up to 4.1 GPa (Figure S8).

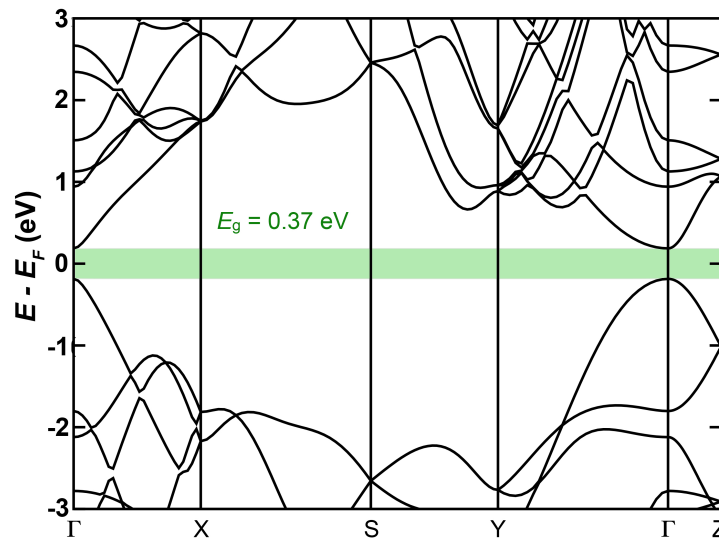


Figure S14: Electronic band structure of bulk black phosphorus at 0 GPa performed using the HSE06 hybrid functional.^{41,42} The direct electronic band gap ($E_g = 0.37$ eV) is obtained at the Γ -point.

Figure S15 shows the hydrostatic pressure dependence of the electronic band gap (E_g), where an increase in pressure reduces the interlayer distances and the E_g reduces linearly with a $\partial E_g / \partial p$ slope of -0.2 eV/GPa. Such change in calculated band gap (E_g) shows that a semiconductor-metal phase transition is occurred at 1.83 GPa and beyond this value BP crystal becomes metallic.

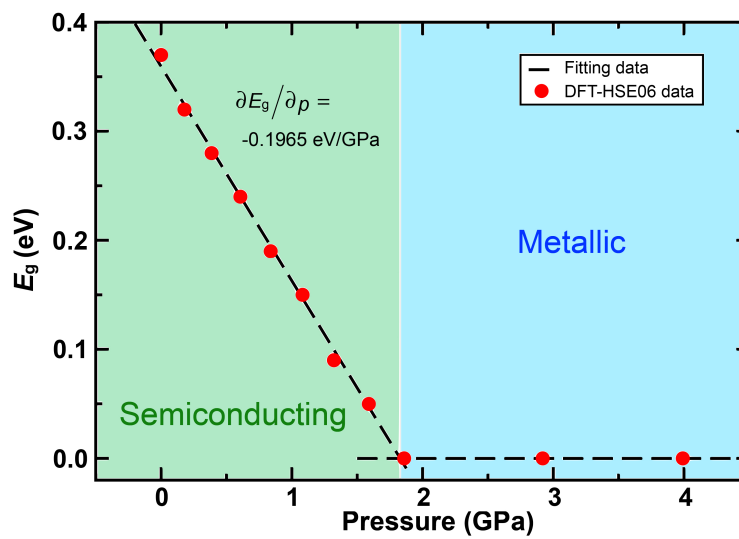


Figure S15: Hydrostatic pressure-dependent electronic band gap for bulk black phosphorus. Semiconductor-metal phase transition occurs at 1.83 GPa. These calculations are performed using the HSE06 hybrid functional.^{41,42}

8 Hydrostatic Pressure Applied on Blue Phosphorus

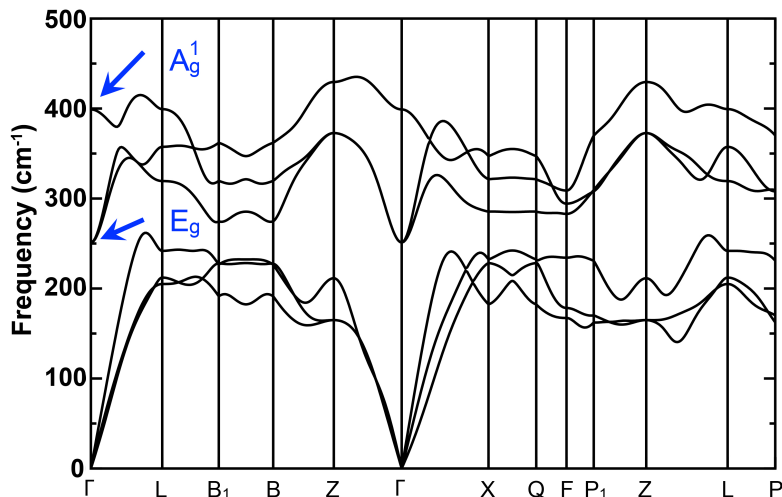


Figure S16: Vibrational band structure of bulk blue phosphorus at 3 GPa. These calculations are based on the hydrostatic pressure method.

9 Methods

9.1 Sample Preparation

The pristine few-layer layered BP flakes are directly micro-mechanically exfoliated using standard scotch-tape method on the diamond surface of DAC from the bulk single crystal, supplied by Manchester Nanomaterials (MN). The exfoliated BP flake is composed of at least 5 layers, which is confirmed by analyzing the Raman spectra, as shown in Figure S3. The transfer and loading of DAC takes less than 10 minutes. The transferred BP flake is covered by the pressure transmitting medium immediately to avoid direct exposure to air. Optical microscopy technique has been used to identified the location of the interested few-layer BP flakes with a 20 \times objective lens.

9.2 Raman Spectroscopy

The Raman scattering measurements were carried out at room temperature using the micro-optical system of a HORIBA LabRAM HR Evolution spectrometer equipped with a 532 nm solid state laser. The laser beam was focused using a long distance 50 \times objective, where the laser power has been kept below 2 mW to avoid thermal heating caused by the laser beam. The Raman spectra was recorded through backscattering geometry and recorded with a 1800 grooves/mm grating, with a spectral resolution of about 0.5 cm⁻¹. The high-pressure Raman spectroscopy was performed using a DAC, having a cutlet with a diameter of \sim 0.8 mm. Methanol: ethanol mixture in 4:1 ratio (ME) has been used as the pressure transmitting medium. Each peak position and linewidth were obtained by fitting the Raman peaks using a Lorentzian function. The peak intensities have been normalized relative to the higher intensity. Here, it is worth mentioning that the viscosity of the PTM liquid is enhanced by a factor of $\sim 10^4$ between 0 to 5 GPa, which suggests the quenching of a strong volume change.⁴³ Due to the strong shape change that associated with the phase transition, both medium ability to transmit hydrostatic stress and diamond cell surface can impose boundary condition deviating from pure hydrostatic stress as with graphene.⁴⁴ The Raman mapping of the sample (Figure S3) was performed using Witec alpha 300R Raman spectrometer.

9.3 Computational Details

We performed first-principles calculations based on DFT. The structural and vibrational properties are carried out using the Vienna *Ab Initio* Simulation Package (VASP).⁴⁵⁻⁴⁸ Ion cores are modeled with projector augmented wave (PAW) pseudopotentials.⁴⁹ The valence 2s and 3p states of phosphorus are treated explicitly. A plane-wave basis energy cutoff of 400 eV and a Gaussian smearing of 0.005 eV were found to yield converged total energy and forces. To include vdW corrections in our calculations, we use the optB86b-vdW scheme.^{50,51}

This particular choice of exchange-correlation functional is based on previous works.⁵² All atoms were relaxed to a force cutoff of 10^{-4} eV.Å⁻¹. In order to determine the equilibrium lattice parameters (at zero temperature and zero pressure) of BP and bP was also allowed to relax. The k -point sampling is based on a Γ -centered grid for all calculations. To optimize the primitive cells, we use $(10 \times 14 \times 7)$ and $(14 \times 14 \times 14)$ grids for BP and bP, respectively. The harmonic phonon calculations are performed using Phonopy code⁵³ with a displacement amplitude equal to 0.03 Å. For the BP and bP, $(4 \times 4 \times 2)$ and $(6 \times 6 \times 6)$ supercells are constructed to ensure convergence of the forces, respectively. VASP was used to compute the force with an electronic energy convergence threshold of 10^{-8} eV. At this stage, we use different k -point grids: $(2 \times 2 \times 2)$ for BP and $(1 \times 1 \times 1)$ for bP. Once $E(V)$ and $p(V)$ are determined and the phonon frequencies are obtained for each system, the thermodynamic quantities can be calculated using the canonical distribution from statistical mechanics. The Helmholtz free energy per P atom can be calculated from:^{54,55}

$$F(V[p], T) = \frac{1}{N} \left\{ E(V[p]) + \sum_{\mathbf{q} \in \text{BZ}, j} \frac{\hbar \omega_{\mathbf{q}, j}(V[p])}{2} + k_{\text{B}} T \sum_{\mathbf{q} \in \text{BZ}, j} \ln \left[1 - \exp \left(-\frac{\hbar \omega_{\mathbf{q}, j}(V[p])}{k_{\text{B}} T} \right) \right] \right\}, \quad (11)$$

for a given pressure p and where N is the number of P atoms. The first term is the ground state energy of each bulk. The second and third terms are the contributions from the zero point and vibrational (entropy) energies, respectively. The sums run over all bands and phonon wave vectors in the first BZ. \hbar and k_{B} are the reduced Planck and Boltzmann constants, respectively. We calculate $F(V[p], T)$ at 0 and 300 K and for several pressure using Phonopy package with a $(100 \times 100 \times 50)$ and $(150 \times 150 \times 150)$ q -point mesh for bulk BP and bP, respectively. The electronic band structure of bulk BP is determined using the HSE06 hybrid functional,^{41,42} based on the atomic structures obtained from the full relaxation by optB88-vdW.^{50,51} At this stage, the Kerker mixing scheme is used. This method has already

been used successfully to study BP's electronic band gap.^{56,57}

References

1. Mao, H.; Xu, J.-A.; Bell, P. Calibration of the ruby pressure gauge to 800 kbar under quasi-hydrostatic conditions. *Journal of Geophysical Research: Solid Earth* **1986**, *91*, 4673–4676.
2. Ling, X.; Liang, L.; Huang, S.; Piretzky, A. A.; Geohegan, D. B.; Sumpter, B. G.; Kong, J.; Meunier, V.; Dresselhaus, M. S. Low-frequency interlayer breathing modes in few-layer black phosphorus. *Nano Lett.* **2015**, *15*, 4080–4088.
3. Lu, W.; Nan, H.; Hong, J.; Chen, Y.; Zhu, C.; Liang, Z.; Ma, X.; Ni, Z.; Jin, C.; Zhang, Z. Plasma-assisted fabrication of monolayer phosphorene and its Raman characterization. *Nano Research* **2014**, *7*, 853–859.
4. Blake, P.; Hill, E.; Castro Neto, A.; Novoselov, K.; Jiang, D.; Yang, R.; Booth, T.; Geim, A. Making graphene visible. *Applied physics letters* **2007**, *91*, 063124.
5. Benameur, M.; Radisavljevic, B.; Héron, J.; Sahoo, S.; Berger, H.; Kis, A. Visibility of dichalcogenide nanolayers. *Nanotechnology* **2011**, *22*, 125706.
6. Roddaro, S.; Pingue, P.; Piazza, V.; Pellegrini, V.; Beltram, F. The optical visibility of graphene: interference colors of ultrathin graphite on SiO₂. *Nano letters* **2007**, *7*, 2707–2710.
7. Wang, Y. Y.; Gao, R. X.; Ni, Z. H.; He, H.; Guo, S. P.; Yang, H. P.; Cong, C. X.; Yu, T. Thickness identification of two-dimensional materials by optical imaging. *Nanotechnology* **2012**, *23*, 495713.
8. Rani, R.; Kundu, A.; Hazra, K. S. Spectral dependent white light reflection mapping of MoS₂ flake for improving accuracy of conventional optical thickness profiling. *Optical Materials* **2019**, *90*, 46–50.

9. Liang, L.; Zhang, J.; Sumpter, B. G.; Tan, Q.-H.; Tan, P.-H.; Meunier, V. Low-Frequency Shear and Layer-Breathing Modes in Raman Scattering of Two-Dimensional Materials. *ACS Nano* **2017**, *11*, 11777–11802, PMID: 29099577.
10. Sun, Y. W.; Holec, D.; Xu, Y.; Dunstan, D. J. Graphite under compression: shift of layer breathing and shear modes frequencies with interlayer spacing. *J. Phys. Commun.* **2018**, *2*, 045004.
11. Yan, Y.; Li, F.; Gong, Y.; Yao, M.; Huang, X.; Fu, X.; Han, B.; Zhou, Q.; Cui, T. Interlayer coupling affected structural stability in ultrathin MoS₂: an investigation by high pressure Raman spectroscopy. *J. Phys. Chem. C* **2016**, *120*, 24992–24998.
12. Xia, J.; Li, D.-F.; Zhou, J.-D.; Yu, P.; Lin, J.-H.; Kuo, J.-L.; Li, H.-B.; Liu, Z.; Yan, J.-X.; Shen, Z.-X. Pressure-Induced Phase Transition in Weyl Semimetallic WTe₂. *Small* **2017**, *13*, 1701887.
13. Ko, P. J.; Abderrahmane, A.; Thu, T. V.; Ortega, D.; Takamura, T.; Sandhu, A. Laser power dependent optical properties of mono-and few-layer MoS₂. *J. Nanosci. Nanotechnol.* **2015**, *15*, 6843–6846.
14. Li, H.; Zhang, Q.; Yap, C. C. R.; Tay, B. K.; Edwin, T. H. T.; Olivier, A.; Baillargeat, D. From bulk to monolayer MoS₂: evolution of Raman scattering. *Adv. Funct. Mater.* **2012**, *22*, 1385–1390.
15. Chakraborty, B.; Gupta, S. N.; Singh, A.; Kuiry, M.; Kumar, C.; Muthu, D. V. S.; Das, A.; Waghmare, U. V.; Sood, A. K. Electron-hole asymmetry in the electron-phonon coupling in top-gated phosphorene transistor. *2D Mater.* **2016**, *3*, 015008.
16. Das, A.; Pisana, S.; Chakraborty, B.; Piscanec, S.; Saha, S. K.; Waghmare, U. V.; Novoselov, K. S.; Krishnamurthy, H. R.; Geim, A. K.; Ferrari, A. C. Monitoring dopants

- by Raman scattering in an electrochemically top-gated graphene transistor. *Nature Nanotech.* **2008**, *3*, 210.
17. Xiang, Z. J.; Ye, G. J.; Shang, C.; Lei, B.; Wang, N. Z.; Yang, K. S.; Liu, D. Y.; Meng, F. B.; Luo, X. G.; Zou, L. J. Pressure-induced electronic transition in black phosphorus. *Phys. Rev. Lett.* **2015**, *115*, 186403.
 18. Gupta, S. N.; Singh, A.; Pal, K.; Chakraborti, B.; Muthu, D. V. S.; Waghmare, U. V.; Sood, A. K. Raman anomalies as signatures of pressure induced electronic topological and structural transitions in black phosphorus: Experiments and theory. *Phys. Rev. B* **2017**, *96*, 094104.
 19. Karuzawa, M.; Ishizuka, M.; Endo, S. The pressure effect on the superconducting transition temperature of black phosphorus. *J. Phys. Condens. Matter* **2002**, *14*, 10759.
 20. Murnaghan, F. D. The compressibility of media under extreme pressures. *Proc. Natl. Acad. Sci. USA PNAS* **1944**, *30*, 244–247.
 21. Birch, F. Finite elastic strain of cubic crystals. *Phys. Rev.* **1947**, *71*, 809.
 22. Cartz, L.; Srinivasa, S. R.; Riedner, R. J.; Jorgensen, J. D.; Worlton, T. G. Effect of pressure on bonding in black phosphorus. *J. Chem. Phys.* **1979**, *71*, 1718–1721.
 23. Brown, A.; Rundqvist, S. Refinement of the crystal structure of black phosphorus. *Acta Crystallogr.* **1965**, *19*, 684–685.
 24. Liu, H.; Du, Y.; Deng, Y.; Peide, D. Y. Semiconducting black phosphorus: synthesis, transport properties and electronic applications. *Chem. Soc. Rev.* **2015**, *44*, 2732–2743.
 25. Cartz, L.; Srinivasa, S.; Riedner, R.; Jorgensen, J.; Worlton, T. Effect of pressure on bonding in black phosphorus. *The Journal of Chemical Physics* **1979**, *71*, 1718–1721.

26. Zhang, J. L.; Zhao, S.; Han, C.; Wang, Z.; Zhong, S.; Sun, S.; Guo, R.; Zhou, X.; Gu, C. D.; Yuan, K. D. Epitaxial growth of single layer blue phosphorus: a new phase of two-dimensional phosphorus. *Nano Lett.* **2016**, *16*, 4903–4908.
27. Gu, C.; Zhao, S.; Zhang, J. L.; Sun, S.; Yuan, K.; Hu, Z.; Han, C.; Ma, Z.; Wang, L.; Huo, F. Growth of quasi-free-standing single-layer blue phosphorus on tellurium monolayer functionalized Au(111). *ACS Nano* **2017**, *11*, 4943–4949.
28. Zhu, Z.; Tománek, D. Semiconducting Layered Blue Phosphorus: A Computational Study. *Phys. Rev. Lett.* **2014**, *112*, 176802.
29. Sasaki, T.; Kondo, K.; Akahama, Y.; Nakano, S.; Taniguchi, T. Raman spectroscopy of two-dimensional material under high pressure: Black phosphorus ultrathin film, phosphorene. *Jpn. J. Appl. Phys.* **2017**, *56*, 05FB06.
30. Akahama, Y.; Kobayashi, M.; Kawamura, H. Simple-cubic–simple-hexagonal transition in phosphorus under pressure. *Phys. Rev. B* **1999**, *59*, 8520.
31. Jamieson, J. C. Crystal structures adopted by black phosphorus at high pressures. *Science* **1963**, *139*, 1291–1292.
32. Scelta, D.; Baldassarre, A.; Serrano-Ruiz, M.; Dziubek, K.; Cairns, A. B.; Peruzzini, M.; Bini, R.; Ceppatelli, M. The p-sc structure in phosphorus: bringing order to the high pressure phases of group 15 elements. *Chem. Commun.* **2018**, *54*, 10554–10557.
33. Tristant, D.; Cupo, A.; Ling, X.; Meunier, V. Phonon Anharmonicity in Few-Layer Black Phosphorus. *ACS Nano* **2019**, *13*, 10456–10468.
34. Jiang, J.-W.; Park, H. S. Negative poisson's ratio in single-layer black phosphorus. *Nat. Commun.* **2014**, *5*, 4727.

35. Fujii, Y.; Akahama, Y.; Endo, S.; Narita, S.; Yamada, Y.; Shirane, G. Inelastic neutron scattering study of acoustic phonons of black phosphorus. *Solid State Commun.* **1982**, *44*, 579–582.
36. Yamada, Y.; Fujii, Y.; Akahama, Y.; Endo, S.; Narita, S.; Axe, J. D.; McWhan, D. B. Lattice-dynamical properties of black phosphorus under pressure studied by inelastic neutron scattering. *Phys. Rev. B* **1984**, *30*, 2410.
37. Jiang, J.-W.; Wang, B.-S.; Park, H. S. Interlayer breathing and shear modes in few-layer black phosphorus. *J. Phys. Condens. Matter* **2016**, *28*, 165401.
38. Warschauer, D. Electrical and optical properties of crystalline black phosphorus. *J. Appl. Phys.* **1963**, *34*, 1853–1860.
39. Maruyama, Y.; Suzuki, S.; Kobayashi, K.; Tanuma, S. Synthesis and some properties of black phosphorus single crystals. *Physica B+ c* **1981**, *105*, 99–102.
40. Narita, S.; Akahama, Y.; Tsukiyama, Y.; Muro, K.; Mori, S.; Endo, S.; Taniguchi, M.; Seki, M.; Suga, S.; Mikuni, A. Electrical and optical properties of black phosphorus single crystals. *Physica B+ c* **1983**, *117*, 422–424.
41. Heyd, J.; Scuseria, G. E.; Ernzerhof, M. Hybrid functionals based on a screened Coulomb potential. *J. Chem. Phys.* **2003**, *118*, 8207–8215.
42. Heyd, J.; Scuseria, G. E.; Ernzerhof, M. Erratum: “Hybrid functionals based on a screened Coulomb potential”[*J. Chem. Phys.* 118, 8207 (2003)]. *J. Chem. Phys.* **2006**, *124*, 219906.
43. Grocholski, B.; Jeanloz, R. High-pressure and-temperature viscosity measurements of methanol and 4: 1 methanol: ethanol solution. *The Journal of chemical physics* **2005**, *123*, 204503.

44. Machon, D.; Bousige, C.; Alencar, R.; Torres-Dias, A.; Balima, F.; Nicolle, J.; de Sousa Pinheiro, G.; Souza Filho, A. G.; San-Miguel, A. Raman scattering studies of graphene under high pressure. *Journal of Raman Spectroscopy* **2018**, *49*, 121–129.
45. Kresse, G.; Hafner, J. *Ab initio* molecular dynamics for liquid metals. *Phys. Rev. B* **1993**, *47*, 558–561.
46. Kresse, G.; Hafner, J. *Ab initio* molecular-dynamics simulation of the liquid-metal–amorphous-semiconductor transition in germanium. *Phys. Rev. B* **1994**, *49*, 14251–14269.
47. Kresse, G.; Furthmüller, J. Efficient iterative schemes for *ab initio* total-energy calculations using a plane-wave basis set. *Phys. Rev. B* **1996**, *54*, 11169–11186.
48. Kresse, G.; Furthmüller, J. Efficiency of *ab-initio* total energy calculations for metals and semiconductors using a plane-wave basis set. *Comput. Mater. Sci.* **1996**, *6*, 15 – 50.
49. Blöchl, P. E. Projector augmented-wave method. *Phys. Rev. B* **1994**, *50*, 17953–17979.
50. Klimeš, J.; Bowler, D. R.; Michaelides, A. Chemical accuracy for the van der Waals density functional. *J. Phys. Condens. Matter* **2009**, *22*, 022201.
51. Klimeš, J.; Bowler, D. R.; Michaelides, A. Van der Waals density functionals applied to solids. *Phys. Rev. B* **2011**, *83*, 195131.
52. Tristant, D.; Cupo, A.; Meunier, V. Finite temperature stability of single-layer black and blue phosphorus adsorbed on Au (111): a first-principles study. *2D Mater.* **2018**, *5*, 035044.
53. Togo, A.; Tanaka, I. First principles phonon calculations in materials science. *Scr. Mater.* **2015**, *108*, 1–5.

54. Pavone, P.; Karch, K.; Schütt, O.; Strauch, D.; Windl, W.; Giannozzi, P.; Baroni, S. *Ab initio* lattice dynamics of diamond. *Phys. Rev. B* **1993**, *48*, 3156.
55. Mounet, N.; Marzari, N. First-principles determination of the structural, vibrational and thermodynamic properties of diamond, graphite, and derivatives. *Phys. Rev. B* **2005**, *71*, 205214.
56. Liu, H.; Neal, A. T.; Zhu, Z.; Luo, Z.; Xu, X.; Tománek, D.; Ye, P. D. Phosphorene: an unexplored 2D semiconductor with a high hole mobility. *ACS Nano* **2014**, *8*, 4033–4041.
57. Qiao, J.; Kong, X.; Hu, Z.-X.; Yang, F.; Ji, W. High-mobility transport anisotropy and linear dichroism in few-layer black phosphorus. *Nat. Commun.* **2014**, *5*, 4475.